Journal of Superconductivity and Novel Magnetism (2025) 38:38
https://doi.org/10.1007/s10948-024-06865-9

RESEARCH

Structural and Mechanical Dynamics of Y-358 Superconductors Influenced by Tb/Y and Zn/Cu Substitutions

O. Ozturk[1] · G. Guducu[1] · S. Kurnaz[2] · T. Seydioglu[3] · S. Safran[4]

Received: 17 July 2024 / Accepted: 9 October 2024 / Published online: 27 December 2024

Abstract

The search for superconductors with superior mechanical properties has driven research into homovalent replacements. In this work, we have systematically incorporated Tb/Y and Zn/Cu dopants into $Y_{3-x}(Tb)_xBa_5Cu_8O_{18-\delta}$ and $Y_3Ba_5Cu_{8-x}(Zn)_xO_{18-\delta}$ based bulk superconductors using the sol-gel technique. Our goal was to explore the fundamental mechanisms linking dopant concentration (0–15%), substitution, processing, and mechanical performance. Understanding these mechanisms can help in designing robust and high-performance superconducting materials for various technological applications. The samples were extensively investigated by X-ray diffraction (XRD), scanning electron microscopy (SEM), Vickers hardness measurements and related calculations. The hardness data were further evaluated using Meyer's law, the proportional sample resistance (PSR) model, the elastic/plastic deformation (EPD) model, the Hays-Kendall (HK) approach, and the indentation-induced cracking (IIC) model. This study reveals the fundamental changes in the properties of Y-358 superconductors due to Tb/Y and Zn/Cu substitutions. The interpretation of the XRD study results leads to the conclusion that all samples have an orthorhombic crystal structure. XRD results confirmed that all samples maintained an orthorhombic crystal structure. However, significant XRD peaks indicated that Tb doping above 10% introduced impurities. Additionally, micromechanical studies demonstrated that hardness values in the plateau region consistently decreased as Tb and Zn doping ratios increased. A decrease in hardness values with increasing applied load, known as the indentation size effect (ISE), was also observed. Among the modeling techniques applied, the IIC model provided the best fit for the hardness test results.

Keywords Y-358 · Sol-gel · SEM · XRD · Vickers · Micromechanical modeling

1 Introduction

Recent advancements in the research of high-temperature superconducting (HTS) wires and films have positioned cuprite-based superconductors at the forefront of innovation. These materials offer substantial potential for various industrial and societal applications [1–3]. To achieve high-quality materials with precise nanoscale control over chemical composition and production techniques, it is essential to thoroughly understand the structural, mechanical, electrical, and magnetic properties of cuprite superconductors.

The production of cuprite-based superconductors is significantly influenced by the synthesis method, the choice of starting materials, and the type of dopant used [4, 5]. Among the various synthesis techniques, wet chemical methods like the sol-gel process have become particularly prominent, especially for bulk applications such as superconducting wires and magnets. The sol-gel method offers several key advantages over traditional solid-state reaction methods, including better compositional homogeneity, higher purity, and precise control over crystallite size at the nanoscale [6]. This method allows for the mixing of components on a molecular level, resulting in powder materials with uniform element distribution, high density, and fine crystallite sizes. However, despite these advantages, XRD analysis of materials produced by the sol-gel method can sometimes reveal

✉ O. Ozturk
oozturk@kastamonu.edu.tr

[1] Department of Electrical & Electronics Engineering, Kastamonu University, 37150 Kastamonu, Türkiye

[2] Central Research Laboratory, Kastamonu University, 37150 Kastamonu, Türkiye

[3] Vocational School, Department of Electronics and Automation, Kastamonu University, 37210 Kastamonu, Türkiye

[4] Department of Physics, Ankara University, 06100 Ankara, Türkiye

impurity peaks [7]. These impurities may arise from various factors, such as incomplete phase formation, the presence of secondary phases, or deviations in critical processing parameters like sintering temperature and duration. While the sol-gel method is effective in promoting the formation of the desired orthorhombic crystal structure, it is crucial to rigorously control these processing conditions to minimize impurity formation. The presence of such impurities can negatively impact the superconducting and mechanical properties of the material, underscoring the importance of optimizing the synthesis process to achieve both high purity and the desired structural characteristics [8–10].

In contrast to conventional solid-state reactions, which typically require high temperatures and extended processing times, often leading to inhomogeneities and larger grain sizes, the sol-gel method operates at relatively lower temperatures and provides superior control over the microstructure of the final product [11]. This is especially crucial for superconductors like Y-358, where maintaining the orthorhombic crystal structure is essential for achieving optimal superconducting properties [12]. The sol-gel process not only facilitates the formation of this desired crystal structure but also minimizes the introduction of impurities during synthesis, resulting in a material with enhanced electrical and mechanical properties. Furthermore, the effectiveness of doping, a critical factor in tailoring the properties of superconductors, is significantly improved through the sol-gel process, as the uniform distribution of dopants ensures more consistent and predictable modifications in the material's characteristics. The selection of starting materials and the specific parameters of the production process, such as sintering temperature, duration, oxygen partial pressure, and applied pressure, are all crucial in determining the superconducting performance of the resulting material [13–15].

For industrial applications of HTSs, mechanical properties such as hardness, elasticity, tensile and fracture strength, and flexibility are as crucial as their superconducting, electrical, magnetic, and microstructural characteristics [16]. Hardness measurement is a non-destructive and widely used method for evaluating the mechanical properties of superconducting materials, offering valuable correlations with other mechanical attributes. The hardness of HTSs is significantly affected by their structure, composition, and production methods [17–19]. The Vickers hardness test is a pivotal technique for assessing the mechanical properties of materials, especially ceramics and brittle compounds like HTSs. This method not only quantifies a material's resistance to deformation but also provides insights into its fracture toughness and brittleness, which are critical factors for practical applications.

Among Y-based superconductors, the $Y_3Ba_5Cu_8O_{18-}\delta$ (Y-358) phase stands out due to its enhanced mechanical robustness compared to the more commonly used $YBa_2Cu_3O_{7-}\delta$ (Y-123) phase. This superior mechanical performance is attributed to Y-358's unique orthorhombic crystal structure, which contributes to increased hardness and fracture toughness, making it highly suitable for applications where both superconducting and mechanical properties are critical. Crystallite size plays a significant role in determining the hardness and strength of materials. According to this principle, reducing the crystallite size leads to an increase in material hardness and yield strength because grain boundaries impede the movement of dislocations—defects in the crystal structure that facilitate deformation [20]. Therefore, controlling crystallite size is crucial for optimizing the mechanical robustness of superconducting materials. The sol-gel method offers precise control over crystallite size at the nanoscale, enabling the synthesis of Y-358 superconductors with tailored properties [6].

The introduction of dopants such as Tb and Zn into the Y-358 superconductor can further enhance its mechanical properties by altering grain boundaries, defect densities, and phase compositions [21, 22]. These modifications influence not only the hardness and elastic modulus but also the material's ability to withstand mechanical stresses. By analyzing the hardness data using various models—such as Meyer's law, the PSR model, the EPD model, the HK approach, and the IIC model—we can gain a deeper understanding of the deformation mechanisms at play. These models help differentiate between elastic and plastic deformation contributions, assess the indentation size effect (ISE), and interpret the material's response to mechanical loads at different scales. In light of these advantages, this study focuses on the Y-358 phase, exploring the potential for further enhancement of its mechanical properties through the doping of Tb and Zn, which are known to influence both the structural and mechanical behaviors of superconducting materials. Understanding how these dopants affect the microstructure and mechanical integrity of Y-358 is crucial for its development and optimization in technological applications that demand high mechanical integrity alongside superior superconducting properties.

In this study, we synthesized undoped, terbium-doped, and zinc-doped Y-358 samples using the sol-gel method. We performed partial substitutions at doping levels of $x = 0.01$, 0.05, 0.10, and 0.15 to replace Y^{3+} ions with Tb^{3+} ions and Cu^{2+} ions with Zn^{2+} ions, respectively. By utilizing the precise control offered by the sol-gel process, we aimed to achieve uniform doping and adjust the microstructure of the Y-358 phase. We thoroughly investigated the structural and mechanical properties of the samples using XRD, SEM, and Vickers hardness measurements to understand how these substitutions affect the material's behavior. The findings from this research could contribute to improving Y-358 superconductors for applications that require both enhanced superconductivity and strong mechanical properties.

2 Materials and Methods

2.1 Sample Preparation

In this study, partial substitution of terbium with yttrium and partial substitution of zinc with copper in four molar percentages (x = 0.01, 0.05, 0.10, 0.15) were realized to obtain one of the superconducting phases of the YBCO family (Y-358 phase). The doping process was carried out using the formulae $Y_{3-x}(Tb)_xBa_2Cu_3O_{18-\delta}$ and $Y_3Ba_5Cu_{8-x}(Zn)_xO_{18-\delta}$. Yttrium (III) acetate hydrate $Y(CH_3CO_2)_3$, barium acetate $Ba(CH_3CO_2)_2$, copper(II) acetate $Cu(CH_3CO_2)_2$, Tb and Zn nanopowders were used to determine the chemical composition of all samples using the sol-gel technique with anhydrous methanol (CH_3OH) as a diluent, glacial acetic acid (CH_3CO_2H) as a solvent, triethanolamine (tri(2-hydroxyethyl)amine) as a thickener and a pH regulator were used to prepare a wet solution with these starting materials. After the pre-treatment of the samples, the powder form was obtained and then the samples were calcined at 850 °C for at least three times for a period of 24 h to obtain nanocrystallites and they were sintered at 930 °C for 24 h at a heating rate of 5 °C/min. The samples were exposed to oxygen for 5 h at a temperature of 500 °C and cooled to room temperature to prepare them for the measurements. The samples produced according to the Tb ratios (x = 0.0, 0.01, 0.05, 0.10, 0.15) doped into Y-358 were named as Y0, YT1, YT5, YT10 and YT15, respectively. The other samples were named as YZ1, YZ5, YZ10 and YZ15, respectively, according to the Zn ratios doped in the Y-358.

2.2 Characterization

The XRD measurements were carried out using a Bruker D8 Advance model X-ray diffractometer at a scan rate of 3°/min between 2θ = 3–90° with CuKα radiation (λ = 1.5406 Å). The crystal structure and phase purity of the samples were determined by analyzing the diffraction patterns. The interplanar distance (*d*) was calculated, and the Miller indices (*hkl*) were obtained from the characteristic peaks in the X-ray diffraction patterns. The lattice parameters of the orthorhombic crystal structure were calculated using the following equation:

$$\frac{1}{d^2} = \frac{h^2}{a^2} + \frac{k^2}{b^2} + \frac{l^2}{c^2} \tag{1}$$

The crystallite size (*D*) was calculated using the Warren-Scherrer formula:

$$D = 0.941\lambda/B\cos\theta \tag{2}$$

where *B* is the corrected full width at half maximum (FWHM) of the diffraction peak, calculated using:

$$B^2 = B_s^2 - B_m^2 \tag{3}$$

Here, B_s is the measured FWHM and B_m is a constant value (0.000007). The orthorhombicity coefficient (δ) was also obtained using:

$$\delta = 100(a - b)/(a + b) \tag{4}$$

where *a* and *b* are lattice constants. The surface morphologies of the bulk ceramic samples were examined using a FEI QUANTA FEQ 250 scanning electron microscope at 10,000× magnification. The Vickers hardness test was employed to characterize the micromechanical properties of the samples. Measurements were conducted using a Shimadzu HVM-2 model hardness tester. A diamond indenter was used to apply five different loads (F = 0.245, 0.490, 0.980, 1.960, 2.940 N) to the smooth surface of the samples for 10 seconds. To minimize errors due to surface roughness and to obtain accurate results, ten indentations were made at different locations for each load value. In the Vickers hardness analysis method, the *d* value, which is the average of the diagonal lengths d_1 and d_2 of the trace left by the diamond indenter tip on the sample. These measurements were then used to calculate the Vickers hardnFess value (H_V) using the following equation:

$$Hv = \frac{2Fsin\left({}^{\alpha}/_{2}\right)}{d^2} \approx 1854.4\left(\frac{F}{d^2}\right) \tag{5}$$

The H_V values obtained by this method were also used to estimate other mechanical properties of the material, such as the modulus of elasticity, yield strength, brittleness index, and fracture toughness. It is important to note that deriving these mechanical properties from hardness measurements is an approximate approach that involves certain assumptions and limitations. The empirical models used provide estimations based on idealized conditions and may not account for all microstructural factors influencing the material's response. The hardness values calculated from the Vickers hardness measurements using Eq. (5) may vary depending on the material's characteristics. The variation of hardness with respect to the applied load is typically described by four distinct behaviors: First, the ISE describes the phenomenon where the measured hardness decreases as the applied load increases. This behavior is generally associated with the increased influence of surface effects and microstructural features at lower loads, involving both elastic and plastic deformation mechanisms. Second, the Reverse Indentation Size Effect (*RISE*) occurs when the measured hardness increases with increasing applied load. This behavior is primarily due

to dominant plastic deformation, where the material may exhibit work hardening or strain hardening at higher loads, and elastic deformation becomes negligible compared to plastic deformation. Third, load-independent hardness behavior is observed when the measured hardness remains constant despite changes in the applied load. This indicates that the material exhibits a consistent response over the range of applied loads, and the indentation size does not significantly affect the hardness measurement. Lastly, in some materials, the hardness values may fluctuate with varying applied loads, showing irregular increases or decreases. This fluctuation can be due to complex deformation mechanisms, anisotropy, microstructural inhomogeneities, or the presence of residual stresses, causing the material's response to change unpredictably with the applied load.

3 Results and Discussion

3.1 XRD Measurements

The general formulae $Y_{3-x}(Tb)_xBa_5Cu_8O_{18-\delta}$ and $Y_3Ba_5Cu_{8-x}(Zn)_xO_{18-\delta}$ (x = 0.01, 0.05, 0.10 and 0.15) were used in the preparation of Tb and Zn-doped Y-358 samples. The XRD patterns of the samples are shown in Fig. 1, with the Miller indices of some important peaks indicated. The diffraction peaks were analyzed to determine the lattice parameters and assess the phase purity of the samples.

The substitution of Y^{3+} (90 pm) ions with Tb^{3+} (92 pm) in the Y-358 phase initially leads to an increase in the *c* parameter due to the larger ionic radius of Tb^{3+}. This expansion is noticeable at lower doping levels. However, as the doping level increases, the *c* parameter starts to increase

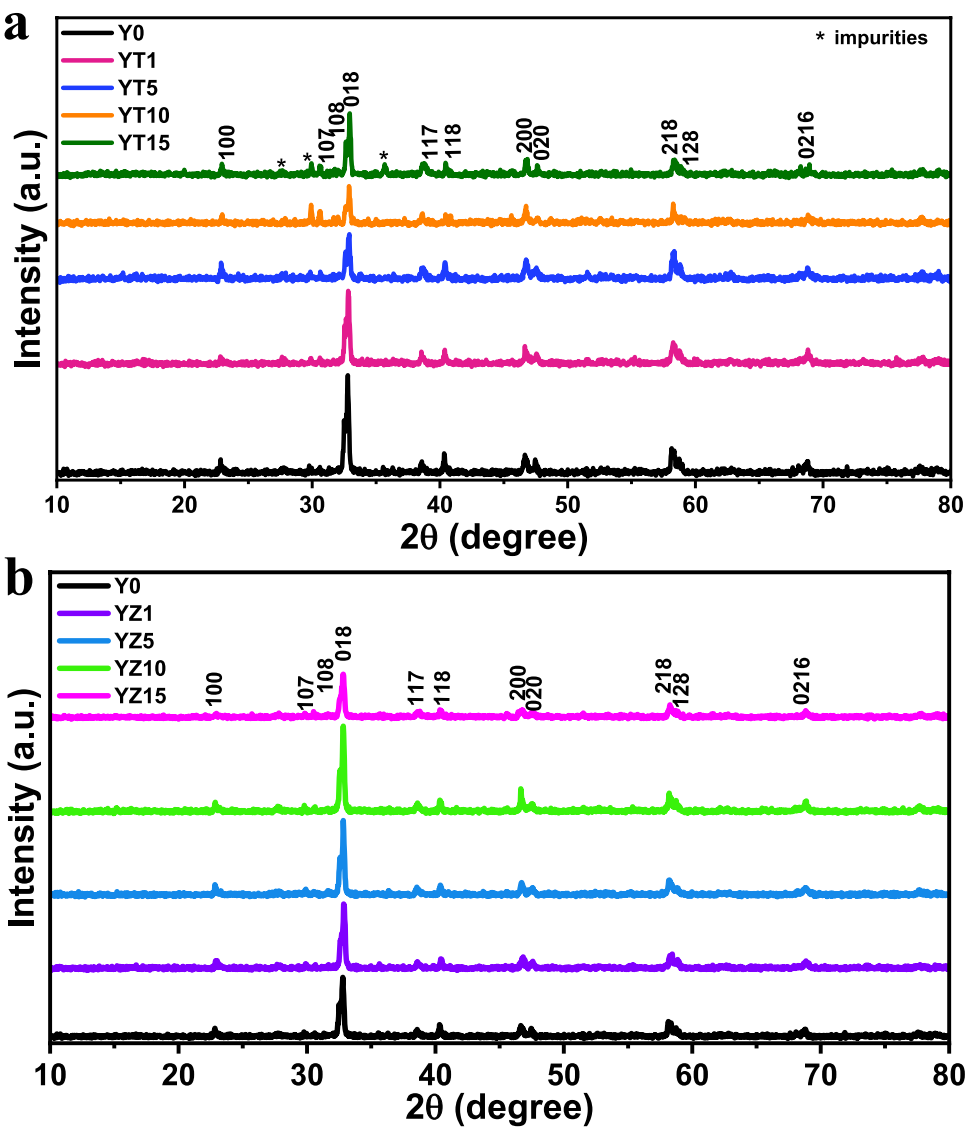

Fig. 1 XRD plot of (**a**) Tb and (**b**) Zn-doped Y-358 samples

and then decrease, likely due to lattice distortions and the formation of secondary phases (Table 1). These distortions and impurities not only affect the structural integrity but also cause a significant reduction in peak intensities, especially at doping levels above 1%. This makes it challenging to maintain a pure orthorhombic structure (Fig. 1a). This trend aligns with other findings in the literature, where increased doping results in complex phase formations and altered lattice parameters [21, 23, 24].

As the doping ratio increases, impurity peaks become more apparent due to secondary phases such as $BaCuO_2$, $BaTbO_3$ and $BaCO_3$. These impurities are observed near the (018) main peak in the XRD pattern. In contrast, Zn doping in Y-358 shows fewer impurities, although small amounts increase with higher doping levels. The Zn^{2+} (74 pm) ion, which replaces Cu^{2+} (73 pm) in the lattice, integrates more smoothly, but still results in a decrease in peak intensities, especially at the 0.15 doping level (Fig. 1b). The ionic radii of the dopants play a crucial role in lattice distortion and secondary phase formation. Tb^{3+}, with a larger ionic radius, causes more significant lattice expansion and strain, particularly along the *c*-axis. Zn^{2+}, with an ionic radius closer to Cu^{2+}, causes less disruption to the lattice. In the Zn-doped samples, a notable decrease in peak intensity is observed at higher doping levels, particularly at 15% Zn doping.

The orthorhombic crystal structure is maintained across all Tb and Zn-doped Y-358 samples, as shown by the characteristic (108)–(018) and (200)–(020) peaks in Table 1. It is also observed that the (108) peak is slightly larger than the (018) peak, and similarly, the (200) peak is larger than the (020) peak. These features confirm the formation of the orthorhombic superconducting phase. However, as the doping level exceeds 1%, there is a noticeable decrease in peak intensities, along with the appearance of impurity peaks [22, 25, 26].

The 10% Zn-doped sample exhibits a well-preserved orthorhombic crystal structure, as evidenced by a high orthorhombicity coefficient (δ =0.872) and the clear, sharp peaks observed in its XRD pattern. However, the (108)–(018) and (200)–(020) peaks are not fully separated, and there is a significant decrease in peak intensities in the 15% Zn-doped sample. Additionally, the crystallite size and unit cell volume of the 15% Zn-doped sample are smaller than those of the other samples. Although there is no significant difference in the lattice parameters a and b, the c parameter is notably lower in the 15% Zn-doped sample. The calculated cell parameters and crystallite sizes for the Zn-doped Y-358 samples align with literature values ($a = 3.88$ Å, $b = 3.82$ Å and $c = 31.01$ Å) [21]. While the crystallite size increases with Zn doping up to 5%, it decreases with further doping. There is also a slight shift of the main peaks towards higher angles as the doping level increases.

Comparing the XRD analysis for all doping ratios in Y-358 phase samples doped with Tb and Zn reveals that the intensity of the main peaks is generally higher for Zn-doped samples compared to Tb-doped ones. In Zn-doped samples, only one or two minor peaks, with low intensity, can be considered as impurity or secondary phase peaks. However, in Tb-doped samples, impurity peaks are more prominent, especially at 10% and 15% doping levels. These impurity peaks are located in the region between 26° and 30°, suggesting that this area is a mix of characteristic Y-358 peaks and impurity peaks. Additionally, an impurity peak is observed at 36°, indicating that as the doping ratio increases, the partial substitution of Tb and Zn becomes increasingly difficult, leading to the formation of impurities such as Y-211, $BaCuO_2$, $BaTbO_3$, and $BaCO_3$ [23–26].This suggests that the XRD pattern of Tb and Zn-doped Y-358 samples is not entirely clean, and the challenge in obtaining a pure Y-358 phase may result in the presence of Y-123 phase impurities. Due to the instability of the Y-358 phase, distinguishing it from Y-123 and Y-112 phases can be challenging based on XRD results [12, 27–30].

3.2 Scanning Electron Microscopy Analyses

The SEM images of the undoped and doped Y-358 samples provide valuable insights into the effects of Tb and Zn

Table 1 Crystallite size, lattice cell parameters and orthorhombicity of Tb and Zn-doped Y-358 samples

Samples	Crystallite size (nm)	*a*(Å)	*b*(Å)	*c*(Å)	*V*(Å^3)	δ
Y0	28.35	3.894	3.831	31.445	469.103	0.812
YT1	29.98	3.894	3.820	31.663	470.953	0.961
YT5	26.06	3.887	3.824	31.688	471.036	0.809
YT10	25.71	3.887	3.815	31.528	467.531	0.928
YT15	25.43	3.889	3.820	31.054	461.337	0.900
YZ1	29.89	3.880	3.822	31.615	468.814	0.749
YZ5	29.04	3.889	3.824	31.662	470.941	0,840
YZ10	28.13	3.894	3.827	31.409	468.010	0.872
YZ15	27.91	3.892	3.829	30.899	460.412	0.812

doping on the microstructure of the Y-358 phase (Figs. 2, 3). In Fig. 2, crystallite distribution, crystallite size and crystallite shape characteristic of the undoped Y-358 phase are shown. The images reveal that the sample lacks a fully planar surface alignment, with some grape-shaped agglomerations observed along the grain boundaries. These partial cumulations suggest localized variations in crystallite growth. Additionally, the presence of partial porous regions within the otherwise dense sample structure may indicate a non-homogeneous crystal formation, possibly due to inconsistencies in the crystallization process.

Figure 3(a–d) show the surface morphologies of the Tb-doped samples (YT1, YT5, YT10, and YT15), while Fig. 3(e–h) present the micrographs for the Zn-doped samples (YZ1, YZ5, YZ10, and YZ15). As Tb doping is introduced at low levels (1% and 5%), there is a noticeable reduction in grain size (Fig. 3a and b). The grains become more uniformly distributed, and the presence of smaller grains suggests that Tb ions are influencing the nucleation and growth processes during synthesis. This reduction in grain size can be attributed to the substitution of Y^{3+} ions with larger Tb^{3+} ions, which introduce lattice distortions and create more nucleation sites, leading to finer grains. At a doping level of 10%, the trend of decreasing grain size continues (Fig. 3c). The grains appear more densely packed, and the grain boundaries become less distinct, indicating enhanced grain boundary cohesion. However, in the YT15 sample (Fig. 3d), a significant change in the microstructure is observed. The grains become irregular in shape and are less uniformly distributed. There is an increase in porosity and the formation of agglomerates or clusters. This distinct microstructure pattern at higher Tb doping levels may be due to the excessive lattice distortions caused by the larger ionic radius of Tb^{3+} ions. The high concentration of Tb ions can lead to the formation of secondary phases or defects, disrupting the grain growth and resulting in an irregular microstructure. The observed microstructural changes in YT15 suggest that while moderate Tb doping can refine the grain size and potentially enhance certain properties, excessive doping may negatively impact the microstructure by promoting defect formation and increasing porosity. This highlights the importance of optimizing the doping level to balance the beneficial and adverse effects on the material's microstructure.

The microstructure of Zn-doped Y-358 samples exhibits different trends compared to the Tb-doped samples. In the YZ1 sample (Fig. 3e), the grains are slightly smaller than those in the undoped sample (Fig. 2a), and there is an increase in porosity. As the Zn doping level increases to 5% and 10%, the grains become more irregular and less interconnected (Fig. 3f and g). There is a noticeable increase in the number of pores and microcracks, indicating that Zn doping at these levels may disrupt the grain growth and cohesion. Interestingly, at the highest doping level of 15% (YZ15), the microstructure appears somewhat improved compared to YZ10 (Fig. 3h). The grains become slightly larger and more uniform, and there is a reduction in porosity and microcracks. This inversion in the microstructural trend suggests that higher Zn doping levels may lead to the formation of a secondary phase or induce a reorganization of the microstructure that mitigates some of the adverse effects observed at intermediate doping levels. The inversion observed in Zn-doped samples could be attributed to the solubility limit of Zn in the Y-358 lattice. At lower doping levels, Zn^{2+} ions substitute for Cu^{2+} ions, leading to lattice distortions and defects that disrupt grain growth. However, at higher doping levels, excess Zn may segregate to grain boundaries or form secondary phases, which could act as a flux and promote grain growth, resulting in larger and more uniform grains.

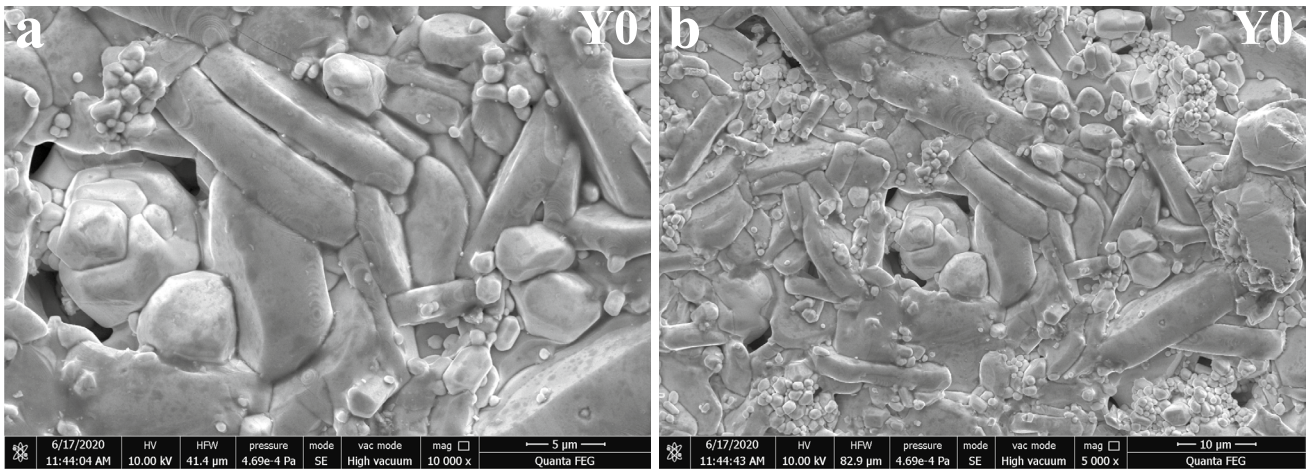

Fig. 2 SEM results of undoped Y-358 samples at a magnification of (**a**) 10,000 and (**b**) 5000

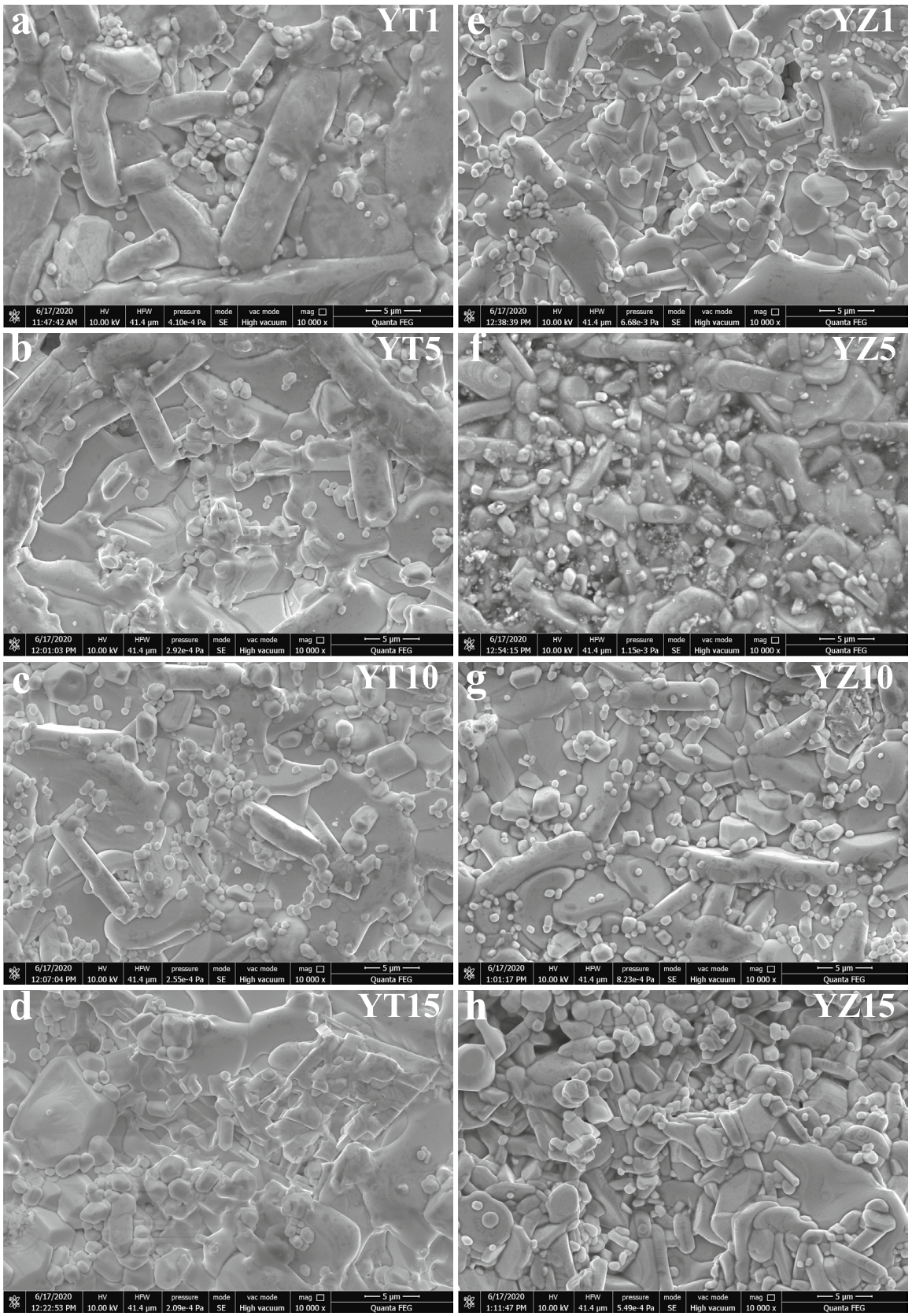

Fig. 3 SEM results of (**a**) YT1, (**b**) YT5, (**c**) YT10, (**d**) YT15, (**e**) YZ1, (**f**) YZ5, (**g**) YZ10, and (**h**) YZ15 samples

In Y-358 samples, as the amount of dopant increases, several microstructural changes are observed. The distance between crystallites widens, grain arrangement becomes more disordered, and bunch-like accumulations appear at the grain boundaries. In Zn-doped samples, the crystallite structure becomes smaller, and the grain boundaries become more irregular. In contrast, Tb-doped samples exhibit the formation of a porous structure as the dopant concentration increases. These microstructural changes, as revealed by SEM images, distinguish Y-358 samples from the Y-123 phase, which typically features a smoother and more uniform grain structure [31].

3.3 Mechanical Properties

The use of Tb and Zn as dopants in Y-358 superconductors was motivated by the distinct effects these elements have on the material's structural and mechanical properties. Tb, with its larger ionic radius compared to Y, was expected to induce lattice distortions that could affect both the superconducting and mechanical behavior of the material. In contrast, Zn, with an ionic radius closer to that of Cu, was anticipated to integrate more smoothly into the lattice, potentially enhancing mechanical robustness without significantly disrupting the superconducting pathways. The results from this study indicate that while both dopants alter the material's hardness and elasticity, they do so in different ways. Tb doping generally leads to a more significant disruption of the lattice, resulting in lower hardness values, whereas Zn doping tends to increase hardness by reducing dislocation mobility. These findings are consistent with previous studies that have explored the role of similar dopants in high-temperature superconductors [32–36].

Hardness measurements on Tb-doped Y-358 superconducting samples prepared by the sol-gel method showed a significant increase in hardness compared to the undoped sample (Fig. 4a). The undoped sample exhibited the lowest hardness value, which decreased as the doping ratio increased. All samples demonstrated ISE behavior, where hardness decreased with increasing applied load. A similar trend was observed in Zn-doped Y-358 samples, where hardness increased with doping (Fig. 4b). However, as the doping level continued to rise, the hardness values of both Tb and Zn-doped samples consistently decreased. This reduction in hardness can be attributed to lattice distortions and the formation of secondary phases caused by the introduction of dopants, which weaken the material's resistance to indentation [37, 38].

The Vickers hardness tests confirmed the ISE behavior across all samples, indicating a decrease in hardness with increasing load, typical of materials undergoing plastic deformation. The consistent ISE behavior suggests that the microstructural integrity of the Y-358 phase is highly sensitive to doping, and the dopants significantly influence the lattice structure. The initial increase in hardness with higher dopant concentrations can be linked to changes in grain boundary characteristics and interactions between the dopants and the Y-358 matrix.

Mechanical characterization of materials involves calculating parameters such as modulus of elasticity (E), fracture strength (K_{IC}), brittleness (B_i) and yield strength (Y) using the Vickers hardness value. The E measures a material's resistance to elastic deformation under an applied load. The value of E depends on the type of material; as E increases, the material becomes less elastic and harder. Therefore, the modulus of elasticity is directly related to the Vickers hardness value and can be calculated using Eq. (7). K_{IC} represents the maximum energy a material can absorb before a crack forms, indicating its ability to undergo plastic deformation. K_{IC} is determined at the point where cracks begin to appear, as described by Eq. (8). B_i measures a material's tendency to resist plastic deformation, with higher B_i values indicating a greater likelihood of permanent deformation, calculated using Eq. (9). Y marks the transition from elastic deformation to plastic deformation and is determined using Eq. (10) [39–41].

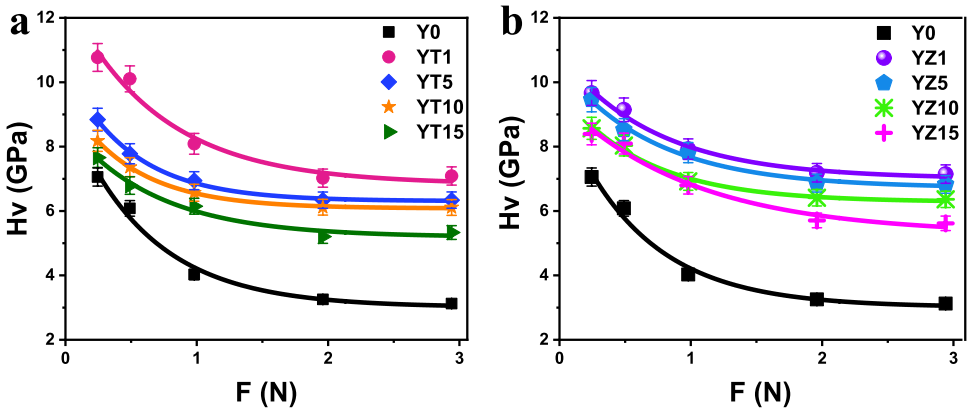

Fig. 4 Hardness of (**a**) Tb and (**b**) Zn-doped Y-358 samples

$$E = 81.9635\, H_V \tag{7}$$

$$K_{IC} = \sqrt{2E\gamma} \tag{8}$$

$$B_i = H_V / K_{IC} \tag{9}$$

$$Y \approx {}^{H_V}/_{3} \tag{10}$$

Tables 2 and 3 present the hardness values of undoped, Tb-doped, and Zn-doped Y-358 samples as a function of the applied load, along with other hardness-related parameters. The undoped Y-358 sample shows the lowest values for hardness, E and K_{IC} across all applied loads. The hardness values of the undoped Y-358 sample are significantly different from those of the doped samples. In other words, the additive had a significant impact on the material's hardness. For Tb-doped samples, the values of E, Y, K_{IC} and B_i consistently decrease as the applied load increases. In contrast, as the Zn doping ratio increases and the applied load increases, the values of E and Y decrease, while K_{IC} and B_i values vary. These results suggest that Zn doping leads to a greater increase in hardness compared to Tb doping, as indicated by the higher hardness values in Zn-doped materials relative to Tb-doped ones. Consistently, the undoped sample exhibits the lowest hardness values across all measurements [42].

3.3.1 Meyer's Law

Meyer's law is one of the methods used to analyze hardness and explain the *ISE/RISE* behavior of materials as a function of applied load. It is expressed as:

$$F = Ad^n \tag{11}$$

where A parameter, related to load-independent hardness, offers additional insight into the material's response to mechanical stress and is detailed in Table 4. The Meyer number n defines both the ISE/RISE behavior and the hardness of a material. When $n < 2$, hardness increases as the applied load decreases, indicating ISE behavior. Conversely, when $n > 2$, hardness increases with applied load, showing RISE behavior [43–46]. If n falls between 1 and 1.6, the material is considered hard, indicating a higher resistance to deformation. On the other hand, if $n > 1.6$, it is considered soft, as it exhibits greater plastic deformation under load.

Table 2 H_V, E, Y, K_{IC} and B_i values of Tb-doped Y-358 samples

Numune	F (N)	d (μm)	H_V (GPa)	H_V Error (± GPa)	E (GPa)	Y (GPa)	K_{IC} (10^{-2} Pa/m$^{1/2}$)	B_i (10^{-2} m$^{1/2}$)
Y0	0.245	8.02	7.057	0.282	578.339	2.352	522.803	1.350
	0.49	12.22	6.083	0.243	498.520	2.028	485.387	1.253
	0.98	21.24	4.029	0.161	330.163	1.343	395.013	1.020
	1.96	33.41	3.256	0.130	266.801	1.085	355.092	0.917
	2.94	41.76	3.126	0.125	256.180	1.042	347.952	0.898
YT1	0.245	6.50	10.770	0.431	882.630	3.590	591.502	1.821
	0.49	9.48	10.105	0.404	828.173	3.368	572.964	1.764
	0.98	14.99	8.089	0.324	662.891	2.696	512.611	1.578
	1.96	22.75	7.023	0.281	575.576	2.341	477.659	1.470
	2.94	27.73	7.090	0.284	581.015	2.363	479.911	1.477
YT5	0.245	7.17	8.840	0.354	724.469	2.947	436.835	2.024
	0.49	10.81	7.781	0.311	637.652	2.594	409.826	1.899
	0.98	16.18	6.944	0.278	569.046	2.315	387.152	1.793
	1.96	23.95	6.339	0.254	519.478	2.113	369.906	1.714
	2.94	29.33	6.339	0.254	519.542	2.13	369.929	1.714
YT10	0.245	7.45	8.179	0.327	670.309	2.726	391.449	2.089
	0.49	11.11	7.364	0.295	603.489	2.455	371.426	1.983
	0.98	16.63	6.569	0.263	538.371	2.190	350.816	1.873
	1.96	24.37	6.119	0.245	501.483	2.040	338.584	1.807
	2.94	29.87	6.112	0.244	500.925	2.037	338.395	1.806
YT15	0.245	7.70	7.660	0.306	627.790	2.553	423.879	1.807
	0.49	11.57	6.793	0.272	556.674	2.264	399.149	1.702
	0.98	17.19	6.149	0.246	503.944	2.050	379.775	1.619
	1.96	26.42	5.207	0.208	426.738	1.736	349.475	1.490
	2.94	31.97	5.333	0.213	437.098	1.778	35.391	1.508

Table 3 H_V, E, Y, K_{IC} and B_i values of Zn-doped Y-358 samples

Samples	F (N)	d (μm)	H_V (GPa)	H_V Error (± GPa)	E (GPa)	Y (GPa)	K_{IC} (10^{-2} Pa/m$^{1/2}$)	B_i (10^{-2} m$^{1/2}$)
Y0	0.245	8.02	7.057	0.282	578.339	2.352	522.803	1.350
	0.49	12.22	6.083	0.243	498.520	2.028	485.387	1.253
	0.98	21.24	4.029	0.161	330.163	1.343	395.013	1.020
	1.96	33.41	3.256	0.130	266.801	1.085	355.092	0.917
	2.94	41.76	3.126	0.125	256.180	1.042	347.952	0.898
YZ1	0.245	6.86	9.666	0.387	792.128	3.222	477.467	2.024
	0.49	9.97	9.146	0.366	749.539	3.049	464.454	1.969
	0.98	15.14	7.924	0.317	649.381	2.641	432.310	1.833
	1.96	22.48	7.190	0.288	589.236	2.397	411.804	1.746
	2.94	27.62	7.149	0.286	585.906	2.383	410.638	1.741
YZ5	0.245	6.93	9.460	0.378	775.301	3.153	474.824	1.992
	0.49	10.32	8.528	0.341	698.871	2.843	450.812	1.892
	0.98	15.25	7.814	0.313	640.409	2.605	431.545	1.811
	1.96	23.01	6.867	0.275	562.776	2.289	404.543	1.697
	2.94	28.26	6.828	0.273	559.615	2.276	403.405	1.693
YZ10	0.245	7.28	8.571	0.343	702.384	2.857	425.859	2.013
	0.49	10.64	8.034	0.321	658.403	2.678	412.310	1.948
	0.98	16.20	6.921	0.277	567.221	2.307	382.696	1.809
	1.96	23.81	6.413	0.257	525.606	2.138	368.390	1.741
	2.94	29.27	6.363	0.255	521.487	2.121	366.944	1.734
YZ15	0.245	7.36	8.393	0.336	687.823	2.798	499.542	1.680
	0.49	10.59	8.097	0.324	663.541	2.699	490.645	1.650
	0.98	16.35	6.801	0.272	557.392	2.267	449.691	1.512
	1.96	25.23	5.709	0.228	467.896	1.903	412.011	1.386
	2.94	31.15	5.619	0.225	460.471	1.873	408.728	1.375

When $n = 2$, hardness becomes independent of the applied load, which corresponds to Kick's Law, expressed as:

$$F = A_{HK} d^2 \tag{12}$$

To analyze the load-independent hardness properties of all samples according to Meyer's law, the n values and lnA values obtained from the lnd-lnF graph in Fig. 5 are used. Since the n of all the samples are less than 2, all the samples exhibit ISE behavior. Doped samples with n values greater than 1.6 are classified as soft, indicating they undergo more plastic deformation under load. In contrast, the undoped sample, with an n value of 1.468, is considered hard, showing resistance to deformation. For both Tb and Zn-doped samples, the n value generally increases with higher doping levels, except at the 15% doping ratio where it slightly decreases. This pattern suggests that, at lower doping levels, the material becomes harder and more prone to plastic deformation. While at higher doping levels, particularly at 15%, the ISE behavior becomes more complex. Tb-doped samples show a strong ISE effect with increasing doping, and a similar trend is observed in Zn-doped samples, with both exhibiting more significant plastic deformation as the doping ratio increases.

Table 4 n and A values of Tb and Zn-doped Y-358 samples

Samples	n	A (GPa)
Y0	1.468	−4.449
YT1	1.676	−4.528
YT5	1.755	−4.881
YT10	1.780	−4.998
YT15	1.725	−4.934
YZ1	1.762	−4.791
YZ5	1.757	−4.811
YZ10	1.768	−4.914
YZ15	1.690	−4.747

3.3.2 Hays-Kendall (HK) Approach

The HK approach proposes a model basedon the minimum load value (W_{HK}) required to cause permanent deformation in a sample [45, 47, 48]. According to this model, if the applied load remains below this threshold, the material undergoes only elastic deformation, with no permanent deformation observed. This model offers valuable insights

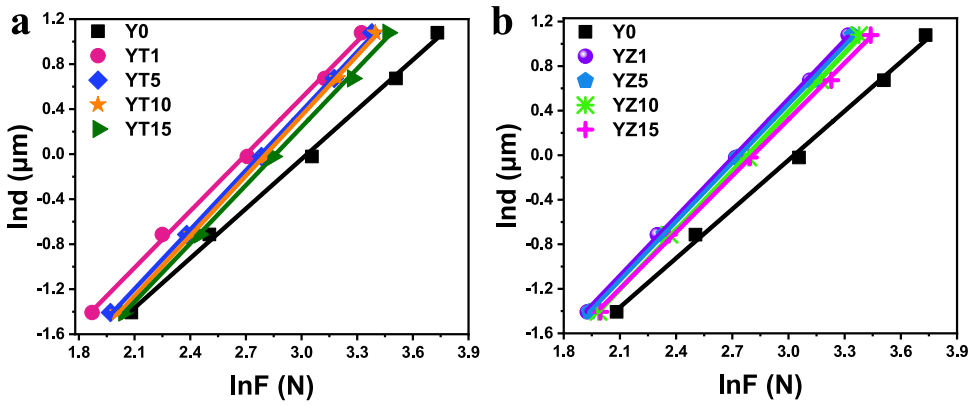

Fig. 5 *lnF* vs. *lnd* graphs of (**a**) Tb and (**b**) Zn-doped Y-358 samples

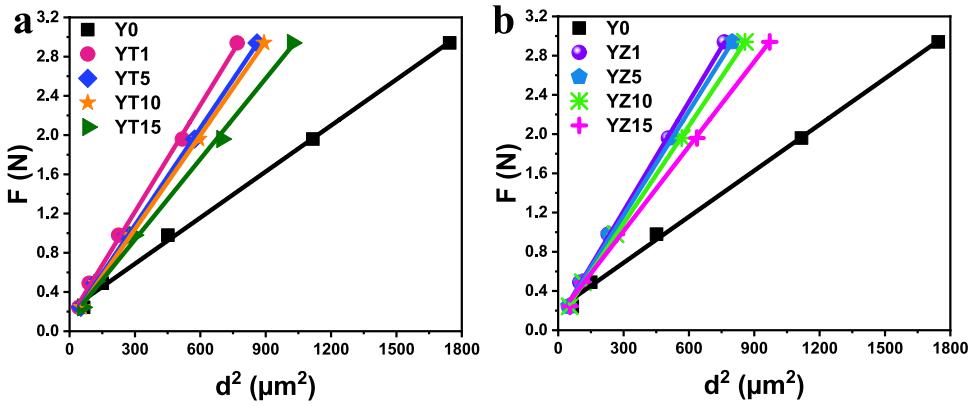

Fig. 6 *F* vs. d^2 graphs of (**a**) Tb and (**b**) Zn-doped Y-358 samples

into how doping influences the microstructural characteristics of the material, which in turn affects its hardness and elastic modulus. The equation proposed by Hays and Kendall to investigate the ISE/RISE behavior of a sample is as follows [48]:

$$F - w_{HK} = A_{HK} d^2 \tag{13}$$

In this equation, A_{HK} represents the load-independent hardness constant. The W_{HK} and A_{HK} values are determined from the F vs. d^2 plot. Specifically, A_{HK} is calculated from the slope of the graph, while W_{HK} is found at the point where the graph intersects the y-axis. The load-independent hardness (H_{HK}) is then calculated using the following equation:

$$H_{HK} = 1.8544\, A_{Hk} \tag{14}$$

This approach allows for the interpretation of load-independent hardness values based on the A_{HK} and W_{HK} values derived from the F-d^2 graph shown in Fig. 6. The calculated A_{HK} values, epresenting the slope of the graph, and W_{HK} values, epresenting the y-intercept, provide insight into the material's compressive strength. The load-independent hardness values calculated using the HK approach are presented in Table 5.

Table 5 A_{HK}, W_{HK} *and* H_{HK} values of Tb and Zn doped Y-358 samples

Sample	A_{HK} (10^{-2} GPa)	W_{HK} (10^{-2} N)
Y0	0.157	21.892
YT1	0.363	13.144
YT5	0.330	9.369
YT10	0.319	8.264
YT15	0.274	11.358
YZ1	0.372	10.109
YZ5	0.354	10.739
YZ10	0.332	9.414
YZ15	0.288	14.756

The W_{HK}, which represents the minimum load required to cause permanent deformation, is positive. A positive W_{HK} value indicates that the material undergoes elastic deformation at the notch tip before any plastic deformation occurs. This phenomenon is well-documented in the literature, where positive W_{HK} are associated with materials that exhibit significant elastic recovery before yielding [48].

Table 5 presents the values of A_{HK}, W_{HK}, and the saturation zone values of H_V. However, the HK approach may not be suitable for analyzing the hardness characteristics of these samples, as the load-independent hardness values calculated

using the HK model differ significantly from the saturation area limits of the actual hardness values for all samples, as shown in Table 9. This discrepancy suggests that the HK model does not accurately capture the complex interactions within the doped Y-358 samples, particularly the effects of doping on the microstructural integrity. The model assumes a simple relationship between applied load and deformation, which may not account for the changes in grain boundaries, secondary phases, or lattice distortions caused by doping. As a result, the HK model might oversimplify the material's mechanical response, leading to inaccurate hardness predictions, especially in heavily doped samples.

3.3.3 Elastic/Plastic Deformation (EPD) Model

In most tests, the size of the notch is measured after the tip of the notch has been extracted from the surface of the sample. Typically, the size of the indentation around the notch decreases to a specific value. To account for this, a correction term has been added to the notch size in load-independent hardness calculations according to the EPD approach [49, 50]. The relationship between the applied load and the notch size in the EPD model is described by Eq. (15):

$$F = A_2\left(d + d_0\right)^2 \tag{15}$$

In this equation, A_2 is a constant, and d_0 represents the correction factor in d. The values of A_2 and d_0 are determined from the graph of the $F^{1/2}$ vs. d plot. Specifically, d_0 is obtained from the y-intercept of the graph, and A_2 is calculated by squaring the slope of the graph. Using this model, load-independent hardness values can be calculated with Eq. (16):

$$H_{EPD} = 1854.4\, A_2 \tag{16}$$

This approach allows for a more accurate determination of hardness by considering the elastic and plastic deformation contributions around the notch, providing a refined analysis of the material's response to applied loads. In this model, the values of A_{EPD}, d_0 and H_{EPD} are calculated from the $F^{1/2}$ vs. d plot shown in Fig. 7. These values, along with the saturation zone values of H_V are given in Table 6. Since the d_0 values are positive for all samples, it indicates that elastic deformation occurs in addition to plastic deformation within the materials. However, the EPD model may not be suitable for this study, as the load-independent hardness values (H_{EPD}) calculated using the EPD model fall outside the saturation zone limits of the Vickers hardness values (Table 9). This discrepancy suggests that the EPD model does not fully capture the true mechanical behavior of the samples under the conditions tested.

3.3.4 Proportional Sample Resistance (PSR) Model

The PSR model is one of the methods used to analyze the ISE/RISE behavior of ceramic materials. According to this model, the resistance of the material increases proportionally with the depth of the notch. The hardness behavior in the PSR approach is defined by the following equation:

$$F = \alpha d + \beta d^2 \tag{17}$$

In this equation, the α parameter represents the load dependence of the Vickers hardness, while the αd term

Table 6 A_{EPD},d_0 and H_{EPD} values of Tb and Zn doped Y-358 samples

Sample	A_{EPD} (10^{-2} GPa)	d_0 (10^{-2} μm)
Y0	0.124	23.843
YT1	0.315	14.602
YT5	0.298	10.525
YT10	0.292	9.375
YT15	0.243	12.411
YZ1	0.336	10.847
YZ5	0.320	11.199
YZ10	0.301	10.331
YZ15	0.252	15.019

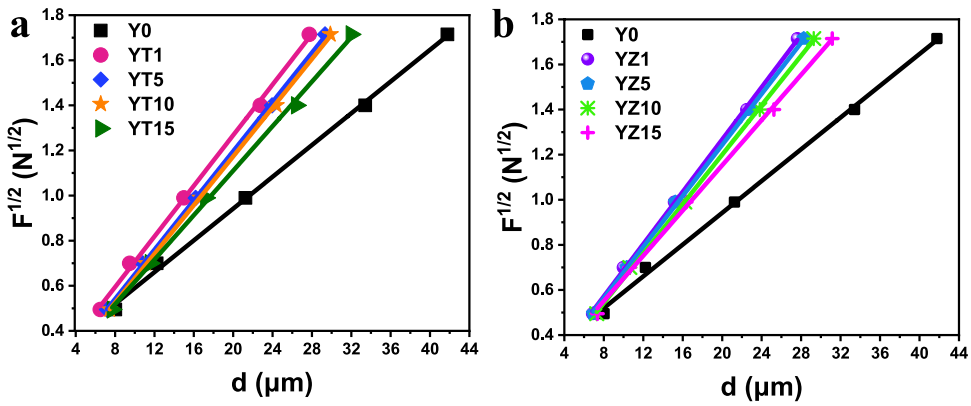

Fig. 7 $F^{1/2}$ vs. d graphs of (**a**) Tb and (**b**) Zn-doped Y-358 samples

describes the surface energy. The α constant is associated with elastic deformation, while the β constant relates to plastic deformation. [49, 51]. The load-independent hardness value in the PSR model is calculated using the following equation:

$$H_{PSR} = 1854.4\ \beta \tag{18}$$

This model enables the determination of hardness by accounting for both elastic and plastic deformation contributions, providing a comprehensive understanding of the material's resistance to indentation. These constants are derived from the F/d vs. d plot, as shown in Fig. 8. The positive α values presented in Table 7 indicate that elastic deformation occurs in conjunction with plastic deformation in the materials. However, it is important to note that the hardness values (H_{PSR}) calculated using the PSR model may not be suitable for this study (Table 9). The H_{PSR} values are outside the saturation range of the true hardness (H_V), suggesting that the PSR model does not fully capture the true mechanical behavior of the Y-358 samples under the conditions tested.

3.3.5 Indentation Induced Cracking (IIC) Model

The Vickers hardness value in the Indentation-Induced Cracking (IIC) model, as defined by Li and Bradt [52], is given by the following equation:

$$H_V = \lambda_1 K_1\left(\frac{F}{d^2}\right) + K_2\left(\frac{F^{5/3}}{d^3}\right) \tag{19}$$

In this equation λ_1, K_1, and K_2 are constants. The constant K_2 depends on the applied load F, while K_1 is determined by the geometric structure of the indenter. For an ideal plastic material, the hardness relationship simplifies to:

$$\lambda_1 = 1\ ve\ K_2\left(F^{5/3}/d^3\right) = 0$$

Thus, the hardness (H_V) equation becomes:

Table 7 α, β and H_{PSR} values of Tb and Zn doped Y-358 samples

Sample	α (10^{-2} N)	β (10^{-2} N/μm)
Y0	2.363	0.109
YT1	1.982	0.304
YT5	1.317	0.293
YT10	1.143	0.288
YT15	1.431	0.238
YZ1	1.439	0.331
YZ5	1.454	0.315
YZ10	1.291	0.296
YZ15	1.814	0.244

$$H_V = K_1\left(F/d^2\right), \tag{20}$$

For an ideal brittle material, where $\lambda_1 = 0$, the hardness relationship is given by:

$$H_V = K_2\left(F^{5/3}/d^3\right) \tag{21}$$

Given that the brittleness of the samples produced in this study is high, the hardness values are calculated using the following equation, derived from the ideal brittle solid model:

$$H_V = K_2\left(\frac{F^{5/3}}{d^3}\right)^m \tag{22}$$

In this equation, K_2 and m are constants calculated from the curves lnH_V vs. $ln(F^{5/3}/d^3)$ graph. The value of m provides insight into the material's hardness characteristics. Specifically, a value of $m > 0.6$ indicates that the material exhibits ISE behavior, while $m < 0.6$ suggests RISE behavior [45, 49, 51].

The calculated m values from the lnH_V vs. $ln(F^{5/3}/d^3)$ plot in Fig. 9 show that since $m > 0.6$ for all samples, indicating that the hardness of the material corresponds to ISE behavior according to the IIC model.

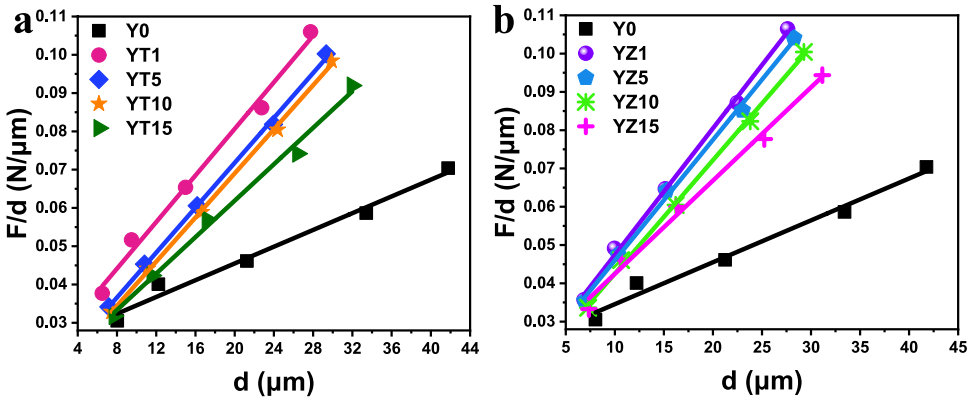

Fig. 8 F/d vs. d graphs of (**a**) Tb and (**b**) Zn-doped Y-358 samples

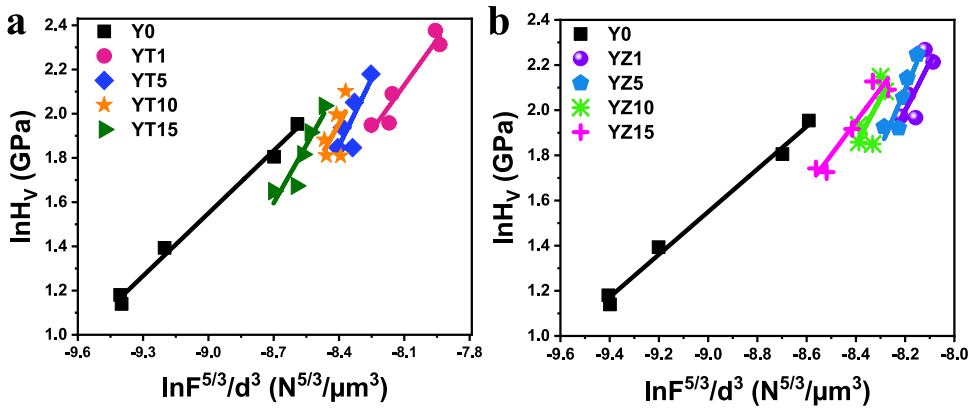

Fig. 9 *ln* H_V vs. *ln* $F^{5/3}/d^3$ graphs of (**a**) Tb and (**b**) Zn-doped Y-358 samples

Table 8 *lnK*, *m* and H_{IIC} values of Tb and Zn doped Y-358 samples

Sample	*lnK* ($N^{(3-5m)/3}/\mu m^{(2-3m)}$)	*m*
Y0	0.945	10.052
YT1	1.368	13.214
YT5	2.037	18.964
YT10	1.794	17.026
YT15	1.751	16.834
YZ1	2.138	19.531
YZ5	2.554	23.034
YZ10	2.029	18.892
YZ15	1.463	14.241

Table 9 Saturation area limit values of H_V and H_{HK}, H_{EPD}, H_{PSR}, H_{IIC} values of Tb and Zn- doped Y-358 samples

Sample	Load independent hardness (modeling)				True hardness (saturation area limits)
	H_{HK} (GPa)	H_{EPD} (GPa)	H_{PSR} (GPa)	H_{IIC} (GPa)	H_V (GPa)
Y0	2.904	2.299	2.030	3.449	4.029–3.126
YT1	6.723	5.837	5.643	7.426	8.089–7.090
YZ1	6.892	6.231	6.130	7.598	7.924–7.149
YT5	6.117	5.528	5.438	6.720	6.944–6.339
YZ5	6.573	5.937	5.837	7.336	7.814–6.828
YT10	5.923	5.411	5.342	6.602	6.569–6.112
YZ10	6.152	5.580	5.495	6.768	6.921–6.363
YT15	5.077	4.513	4.414	5.690	6.149–5.333
YZ15	5.341	4.666	4.517	6.102	6.801–5.619

Table 8 presents the *m* and *lnK* values calculated for all samples. Additionally, Table 9 compares the load-independent H_{IIC} values obtained from the IIC model with the saturation ranges of the load-dependent Vickers hardness values. The H_{IIC} values fall within the saturation limits of the true hardness, indicating that the IIC model provides an accurate and reliable framework for analyzing the hardness characteristics of Tb and Zn-doped Y-358 superconductor samples. This alignment between the H_{IIC} values and the actual hardness data suggests that the IIC model effectively captures the material's response to indentation, making it the most appropriate model for evaluating the mechanical properties of these doped superconductors.

Table 9 presents a comparison between the saturation zone limits of the Vickers hardness values, the H_V value, and the load independent hardness values calculated according to the H_{HK}, H_{EPD}, H_{PSR}, H_{IIC} models for Tb and Zn-doped Y-358 samples. Among these models, only the H_{IIC} values fall within the saturation zone of the Vickers hardness values, indicating that the IIC model is the most suitable for accurately capturing the hardness characteristics of both Tb and Zn-doped Y-358 samples. The results highlight that the IIC model provides a more reliable framework for analyzing the mechanical properties of these doped superconductors. In particular, when comparing Tb and Zn doping, it is evident that the addition of Zn to the Y-358 phase increases the material's hardness more significantly than the addition of Tb. This difference suggests that Zn doping enhances the material's resistance to deformation more effectively, making the Zn-doped Y-358 samples harder compared to their Tb-doped counterparts. The suitability of the IIC model across both doping scenarios underscores its effectiveness in evaluating the complex interactions within the microstructure of these materials.

The results obtained for the Y-358 superconducting phase in our study are particularly significant when compared to the Y-123 phase due to the challenges in synthesizing a pure Y-358 phase, its higher critical temperature, and its relatively recent discovery. Consequently, studies aimed at determining the mechanical properties of the Y-358 phase are essential for better characterizing this superconductor. Moreover, our use of the sol-gel method to produce the Y-358 phase allows us to compare our results with those obtained using the most common production method—the solid-state reaction method.

In Table 10, we compare our results with those from previous studies on the Y-123 and Y-358 phases, including H_V values derived from various hardness models, despite limited data availability. Based on these comparisons, it has been observed that samples produced via the solid-state method generally exhibit *RISE* hardness behavior, or that the *RISE* behavior observed in undoped samples transforms into *ISE* behavior upon doping [18]. In contrast, samples produced by the sol-gel method have higher H_V values compared to those obtained using the solid-state reaction method. The type and amount of doping, production method, and processing conditions significantly influence these values. According to the results of the studies included in Table 10, two studies found that the *IIC* model (similar to our findings) corresponds well with the saturation region values of the actual hardness, while one study found that the *PSR* model aligns with the experimental data. This can be attributed to the presence of some elastic deformation in addition to plastic deformation in the material. Specifically, the smoother surface morphology and grain arrangement on the material's surface, compared to its interior, result in higher resistance to applied loads at the surface. Conversely, inhomogeneities, impurities, increased porosity, and irregularities in grain connections within the bulk can lead to a decrease in hardness with increasing load until saturation is reached, explaining the *ISE* behavior exhibited by the sample. These observations highlight how the synthesis method and microstructure influence the mechanical behavior of superconducting materials; specifically, the higher hardness values in sol-gel synthesized samples suggest that this method may enhance mechanical properties compared to the solid-state reaction method, possibly due to improved microstructural features like reduced porosity and more uniform grain distribution [53].

4 Conclusion

In this study, we investigated the incorporation of Tb/Y and Zn/Cu dopants into the Y-358 superconductor to conduct a comparative analysis of their effects. All samples maintained an orthorhombic crystal structure, but XRD

Table 10 Comparative analysis of hardness values and models forY-358 and Y-123 superconductors produced by sol-gel and solid-state methods

Sample	Method	Load independent hardness (modeling)					True hardness	Ref.
		Meyer number	H_{HK} *(GPa)*	H_{EPD} (GPa)	H_{PSR} (GPa)	H_{IIC} (GPa)	H_V (GPa)	
Und. Y-123	SS	2.25 RISE	3.91	4.31	4.26	3.39	3.42–3.75	[18]
$CoFe_2O_4$/Cu sub. Y-123	SS	1.87–1.91 ISE	3.15–3.41	3.03–3.25	3.02–3.24	3.32–3.73	3.19–3.70	[18]
Und. Y-123	Sol-gel	2.66 RISE	4.52	5.73	5.43	3.41	3.60–4.12	[18]
$CoFe_2O_4$/Cu sub. Y-123	Sol-gel	1.80–1.83 ISE	3.28–4.06	3.02–3.78	2.98–3.74	3.73–4.54	3.38–4.49	[18]
Und. Y-123	SS	1.67 ISE	2.75	2.42	3.04	–	3.01	[54]
CNTs added Y-123	SS	1.67–1.72 ISE	3.07–3.72	2.70–3.36	3.22–4.02	–	3.26–4.04	[54]
Und. Y-123	SS	2.75 RISE	5.37	–	6.58	4.79	4.78–4.82	[55]
Au/Cu sub. Y-123	SS	2.54–3.32 RISE	2.63–4.01	–	3.20–4.71	2.10–3.69	3.15–3.71	[55]
Und. Y-358	SS	RISE	–	–	–	–	6.80–7.60	[56]
Co/Cu sub. Y-358	SS	RISE	–	–	–	–	5.22–6.61	[56]
Und. Y-358	Sol-gel	1.46 ISE	2.90	2.29	2.03	3.44	4.029–3.126	Our work
Tb/Y sub. Y-358	Sol-gel	1.67–1.76 ISE	6.72–5.07	5.83–4.51	5.64–4.41	7.42–5.69	8.08–5.33	Our work
Zn/Cu sub. Y-358	Sol-gel	1.69–1.76 ISE	6.89–5.34	6.23–4.66	6.13–4.51	7.59–6.10	7.92–5.61	Our work

*und. = undoped, subs. = substituted, SS=Solid state

analysis revealed background noise and additional peaks, indicating the presence of impurities. Notably, in samples with 10% and 15% Tb doping, small impurity peaks were identified, likely corresponding to Y-211, $BaCuO_2$, $BaCO_3$, and $BaTbO_3$ phases. The partial substitution of Tb/Y and Zn/Cu into the Y-358 phase resulted in varying effects on the crystal structure. Tb, with a larger ionic radius than Y, caused lattice distortions, while Zn, with an ionic radius similar to Cu, integrated more smoothly into the crystal lattice. Despite changes in XRD peak intensities, the orthorhombic structure was largely preserved, especially in Zn-doped samples. The XRD and SEM analyses provided consistent findings. Both techniques showed that increasing the doping level led to a decrease in grain size and an increase in impurity accumulation at grain boundaries. This resulted in higher porosity and irregularity in the crystallite structure, particularly in Zn-doped samples. However, Tb-doped samples displayed slightly better surface texture and denser structure compared to Zn-doped ones.

Hardness tests using the Vickers method revealed that all samples exhibited *ISE* behavior, with hardness decreasing as the applied load increased. Zn-doped samples were found to be harder than Tb-doped ones, likely due to the more effective integration of Zn^{2+} ions into the crystal lattice, which reduced dislocation movement and enhanced hardness. The mechanical property analyses showed that Zn doping resulted in greater hardness compared to Tb doping. This difference can be attributed to the atomic structures and sizes of the Tb^{3+} and Zn^{2+} ions. The larger ionic radius of Tb^{3+} caused more significant lattice distortions, leading to a reduction in hardness, while Zn^{2+} integrated more effectively, maintaining lattice integrity and enhancing hardness. It is important to note that the E, Y, K_{IC} and B_i were estimated from hardness measurements using empirical models. Finally, among the various models used to calculate load-independent hardness values Meyer's law, PSR model, EPD model, HK approximation, and IIC model. The IIC model was found to be the most accurate in describing the hardness properties of the samples, as it closely matched the experimental H_V data within the saturation zone. This suggests that the IIC model is suitable for analyzing the hardness behavior of doped Y-358 superconductors under the conditions studied.

Author Contribution O.O.,G.G., S.K., and T.S. conceived the idea for the project and designed the experiments. O.O., G.G., S.K. and S.S. performed methodology, project administration, investigation also performed materials production. S.K., G.G. and O.O. performed experimental measurement and resources, formal analysis, review & editing. O.O., S.S., TS, and S.S. performed writing - original draft, writing - review & editing. All authors discussed the results and commented on the manuscript.

Data Availability No datasets were generated or analyzed during the current study.

Declarations

Competing Interests The authors declare no competing interests.

References

1. Shiohara, Y., Yoshizumi, M., Takagi, Y., Izumi, T.: Future prospects of high T_c superconductors-coated conductors and their applications. Physica C. **484**, 1–5 (2001)
2. Murakami, M.: Measurements of trapped-flux density for bulk high-temperature superconductors. Physica C. **357–360**, 751–754 (2001)
3. Hull, J.R.: Superconducting bearings. Supercond. Sci. Technol. **13**(2), R1–R15 (2000)
4. Hench, L.L., West, J.K.: The sol-gel process. Chem. Rev. **90**(1), 33–72 (1990)
5. Nisenoff, M.: Superconducting electronics: current status and future prospects. Cryogenics. **28**(1), 47–56 (1988)
6. Tohge, N., Tatsumisago, M., Minami, T.: Preparation of high-Tc superconducting oxide films in the bi-(Pb)-ca-Sr-cu-O system from stabilized metal-alkoxides. J. Non-Cryst. Solids. **121**(1–3), 443–447 (1990)
7. Brinker, C.J., Scherer, G.W.: Sol-Gel Science: the Physics and Chemistry of sol-Gel Processing. Academic Press (2013)
8. Dihom, M.M., Shaari, A.H., Baqiah, H., Al-Hada, N.M., Chen, S.K., Azis, R.S., Abd-Shukor, R.: Effects of calcination temperature on microstructure and superconducting properties of Y123 ceramic prepared using thermal treatment method. Solid State Phenom. **268**, 325–329 (2017)
9. Livage, J., Henry, M., Sanchez, C.: Sol-gel chemistry of transition metal oxides. Prog. Solid State Chem. **18**(4), 259–341 (1988)
10. Livage, J.: Sol-gel process. Curr. Opin. Solid State Mater. Sci. **2**, 132–138 (1997)
11. Niederberger, M.: Nonaqueous sol–gel routes to metal oxide nanoparticles. Acc. Chem. Res. **40**(9), 793–800 (2007)
12. Khosroabadi, H., Rasti, M., Akhavan, M.: Structural analysis of $Y_3Ba_5Cu_8O_{19-\delta}$ high-T_c superconductor by ab initio density functional theory. Physica C. **497**, 84–88 (2014)
13. Page, C.J., Houk, C.S., Burgoine, G.A.: Sol-gel synthesis of $YBa_2Cu_3O_{7-\delta}$ using yttrium, barium and copper polyether alkoxide precursors. MRS Proc. **271**, (1992)
14. Palacín, M.R., Casañ-Pastor, N., Gómez-Romero, P.: Sol–gel synthesis and simultaneous oxidation of $Ln_2Ba_2Cu_2Ti_2O_{11-\delta}$. J. Solid State Chem. **138**(1), 141–148 (1998)
15. Sen, D., Mitra, A., Ghatak, S.K.: Field dependence and hysteresis effects of harmonic responses of a superconducting Y-Ba-cu-O composite. Supercond. Sci. Technol. **5**(8), 467–471 (1992)
16. Buckel, W., Kleiner, R.: Superconductivity: Fundamentals and Applications, 2nd edn. Wiley-VCH Verlag, Weinheim (2004)
17. Koralay, H., Arslan, A., Cavdar, Ş., Öztürk, Ö., Asikuzun, E., Günen, A., Tasci, A.T.: Structural and mechanical characterizations of $Bi_{1.75}Pb_{0.25}Sr_2Ca_2Cu_{3-x}Sn_xO_{10+}\delta$ superconductor ceramics using Vickers hardness test. J. Mater. Sci. Mater. Electron. **24**, 4270–4278 (2013)
18. Aşıkuzun Tokeşer, E., Bulut, F., Nefrow, A., Seydioglu, T., Kurnaz, S.: The mechanical modelling of $CoFe_2O_4$ doped Y123 superconductor. J. Adv. App. Sci. **2**(1), 1–14 (2023)
19. Kölemen, U., Çelebi, S., Karal, H., Öztürk, A., Çevik, U., Nezir, Görür, O.: Superconducting and Vickers hardness properties of

ZnO-added YBCO polycrystalline superconductors. Phys. Status Solidi B. **241**(2), 274–283 (2004)
20. Hilgenkamp, H., Mannhart, J.: Grain boundaries in high-T_c superconductors. Rev. Mod. Phys. **74**(2), 485–549 (2002)
21. Aliabadi, A., Akhavan Farshchi, Y., Akhavan, M.: A new Y-based HTSC with T_c above 100K. Physica C. **469**(22), 2012–2014 (2009)
22. Manju, P., Rajak, N.K., Alex, A.P., Kamble, V.B., Jaiswal-Nagar, D.: Orthorhombic crystal structure and oxygen deficient cluster distribution model for $YBa_2Cu_{3-x}A_{lx}O_{6+\delta}$ superconductor. Sci. Rep. **10**(1), 7814 (2020)
23. West, A.R.: Solid State Chem. Appl. Wiley (2014)
24. Shannon, R.D.: Revised effective ionic radii and systematic studies of interatomic distances in halides and chalcogenides. Acta Crystallogr. Sect. A. **32**(5), 751–767 (1976)
25. Gholipour, S., Daadmehr, V., Rezakhani, A.T., Khosroabadi, H., Shahbaz Tehrani, F., Hosseini Akbarnejad, R.: Structural phase of Y358 superconductor: comparison with Y123. J. Supercond. Nov. Magn. **25**(7), 2253–2258 (2012)
26. Howe, B.A.: Crystal Structure and Superconductivity of $YBa_2Cu_3O_{7-x}$. Master of Science Theses in Physics. Minnesota State University, Mankato, Minnesota (2014)
27. Almessiere, M.A., Slimani, Y., Hannachi, E., Algarni, R., Ben Azzouz, F.: Impact of Dy_2O_3 nanocrystallites additions on the properties of porous YBCO ceramics. J. Mater. Sci. Mater. Electron. **30**(19), 17572–17582 (2019)
28. Khorramshahi, M., Mohammadizadeh, M.R.: $Y_3Ba_5Cu_8O_x$ superconductor under hydrostatic pressure. J. Low Temp. Phys. **203**(3–4), 309–318 (2021)
29. Tavana, A., Akhavan, M.: How T_c can go above 100 K in the YBCO family. Eur. Phys. J. B. **73**, 79–83 (2010)
30. Udomsamuthirun, P., Kruaehong, T., Nikamjon, T., Ratreng, S.: The new superconductors of YBaCuO materials. J. Supercond. Nov. Magn. **23**, 1377–1380 (2010)
31. Başoğlu, M., Düzgün, İ., Öztürk, A.: Specification of some superconductivity parameters by adding lutetium to the YBCO(358) ceramic superconductor. J. Supercond. Nov. Magn. **34**, 1077–1084 (2021)
32. Jinyu, H., Yuchen, W., Wenhao, L., Yanhan, Z., Xiongfang, L., Difan, Z., Yibing, Z., Xin, Y., Chuanbing, C.: Effects of Zn doping on superconducting properties of melt textured Y–Ba–cu–O bulk superconductors. Supercond. Sci. Technol. **35**, 7 (2022)
33. Guducu, G., Ozturk, Ö., Kurnaz, S., Asıkuzun Tokeser, E., Safran, S., Yıldırım, G.: Assessment of superconducting and structural stability of advanced Y-123 and Y-358 ceramics with Tb/Y substitution in main matrices. J. Alloys Compd. **997**, 174838 (2024)
34. Kazakov, S.M., Angst, M., Karpinski, J., Fita, I.M., Puzniak, R.: Substitution effect of Zn and cu in MgB2 on Tc and structure. Solid State Commun. **119**(1), 1–5 (2001)
35. Loh, S.K., Chuah, S.C., Tran, H.T.T., Abd-Shukor, R., Chong, T.V.: Effect of Ni and Zn substitution on the physical and electrical properties of $NdBaSrCu_3O_{7-\delta}$ high temperature superconductor. Mod. Phys. Lett. B. **37**, 22 (2023)
36. Khan, N.A., Arif, Y., Mumtaz, M., Khurram, A.A.: Comparison of the superconducting properties of $Cu_{0.5}Tl_{0.5}Ba_2Ca_2(Cu_{3-y}Zn_y)O_{10-\delta}$ prepared at different synthesis temperatures. Ceram. Int. **38**(8), 6417–6422 (2012)
37. Meyers, M.A., Chawla, K.K.: Mechanical Behavior of Materials. Cambridge University Press (2009)
38. Tabor, D.: The Hardness of Metals. Oxford University Press (2000)
39. Veerender, C., Dumke, V.R., Nagabhooshanam, M.: Hardness and elastic moduli of $Bi_{2-x}PbxCa_2Sr_2Cu_3O_7$ superconductors. Phys. Status Solidi A. **144**(2), 299–309 (1994)
40. Dogruer, M., Yildirim, G., Ozturk, Ö., Belenli, İ., Terzioglu, C.: Variation of mechanical properties of Cr-doped bi-2212 superconductors. J. Supercond. Nov. Magn. **26**(9), 2949–2954 (2013)
41. Cetinkara, H.A., Yilmazlar, M., Ozturk, Ö., Nursoy, M., Terzioglu, C.: The influence of cooling rates on microstructure and mechanical properties of $Bi_{1.6}Pb_{0.4}Sr_2Ca_2Cu_3Oy$ superconductors. J. Phys. Conf. Ser. **153**, 012038 (2009)
42. Zalaoglu, Y., Karaboga, F., Terzioglu, C., Yildirim, G.: Improvement of mechanical performances and characteristics of bulk bi-2212 materials exposed to au diffusion and stabilization of durable tetragonal phase by au. Ceram. Int. **43**(9), 6836–6844 (2017)
43. Quinn, J.B., Quinn, G.: Indentation brittleness of ceramics: a fresh approach. J. Mater. Sci. **32**(16), 4331–4346 (1997)
44. Ozturk, Ö., Cetinkara, H.A., Asikuzun, E., Akdogan, M., Yilmazlar, M., Terzioglu, C.: Investigation of mechanical and superconducting properties of iron diffusion-doped bi-2223 superconductors. J. Mater. Sci. Mater. Electron. **22**(9), 1501–1508 (1997)
45. Tosun, M., Ataoglu, S., Arda, L., Ozturk, Ö., Asikuzun, E., Akcan, D., Cakiroglu, O.: Structural and mechanical properties of ZnMgO nanocrystallites. Mater. Sci. Eng. A. **590**, 416–422 (2014)
46. Toplu, A., Karaca, İ., Kölemen, U.: Calculation of true hardness value of Zn-added (BiPb)SrCaCuO superconductor by different models. Ceram. Int. **41**(1), 953–960 (2015)
47. Rahal, H.T., Awad, R., Gaber, A.M.A., Roumie, M.: Superconducting and mechanical properties of the bulk $(SnO_2)_x(Bi_{1.6}Pb_{0.4})Sr_2Ca_2Cu_3O_{10-\delta}$ prepared at different sintering times. J. Supercond. Nov. Magn. **30**, 1971–1980 (2017)
48. Hays, C., Kendall, E.G.: An analysis of Knoop hardness. Metallography. **6**(4), 275–282 (1973)
49. Bull, S.J., Page, T.F., Yoffe, E.H.: An explanation of the indentation size effect in ceramics. Philos. Mag. Lett. **59**(6), 281–288 (1989)
50. Asikuzun, E., Ozturk, Ö., Arda, L., Akcan, D., Senol, S.D., Terzioglu, C.: Preparation, structural and micromechanical properties of (Al/mg) co-doped ZnO nanocrystallites by sol–gel process. J. Mater. Sci. Mater. Electron. **26**(10), 8147–8159 (2015)
51. Sangwal, K.: On the reverse indentation size effect and hardness measurement of solids. Mater. Chem. Phys. **63**(2), 145–152 (2000)
52. Li, H., Han, Y.H., Bradt, R.C.: Knoop hardness of single crystal sulfur. J. Mater. Sci. **29**(21), 5641–5645 (1994)
53. Atkins, A.G., Mai, Y.W.: Elastic and Plastic Fracture: Metals, Polymers, Ceramics, Composites, Biological Materials. Halsted Press, Ellis Horwood (1985)
54. Sahoo, B., Routray, K.L., Mirdha, G.C., Singh, A.K., Samal, D., Behera, D.: Investigation of microhardness and superconducting parameters of CNTs blended YBCO superconductor. Ceram. Int. **45**, 22055–22066 (2019)
55. Terzioglu, R., Altintas, S.P., Varilci, A., Terzioğlu, C.: Modeling of Micro-hardness in the au-doped YBCO bulk superconductors. J. Supercond. Nov. Magn. **32**, 3377–3383 (2019)
56. Ozturk, O., Arebat, R.A.M., Nefrow, A.R.A., Bulut, F., Guducu, G., Asikuzun, E., Celik, S.: Investigation of structural, superconducting and mechanical properties of co/cu substituted YBCO-358 ceramic composites. J. Mater. Sci. Mater. Electron. **30**, 7400–7409 (2019)